



# Large deflection analysis of functionally graded carbon nanotube-reinforced composite plates by the element-free $kp$ -Ritz method



Z.X. Lei<sup>a,b,c</sup>, K.M. Liew<sup>a,c,\*</sup>, J.L. Yu<sup>b,c</sup>

<sup>a</sup> Department of Civil and Architectural Engineering, City University of Hong Kong, Kowloon, Hong Kong

<sup>b</sup> CAS Key Laboratory of Mechanical Behavior and Design of Materials, University of Science and Technology of China, PR China

<sup>c</sup> USTC-CityU Joint Advanced Research Centre, Suzhou, Jiangsu, PR China

## ARTICLE INFO

### Article history:

Received 17 October 2012

Received in revised form 11 December 2012

Accepted 18 December 2012

Available online 27 December 2012

### Keywords:

Nonlinear

Carbon nanotube

Composite

First order shear deformation theory

Element-free

$kp$ -Ritz

## ABSTRACT

A nonlinear analysis is presented for functionally graded carbon nanotube-reinforced composite (FG-CNTRC) plates using the element-free  $kp$ -Ritz method. The nonlinear governing equations are developed to investigate problems related to small strains and moderate rotations, based on the first-order shear deformation plate theory and von Kármán strains. Two-dimensional displacement fields of the plates are approximated by a set of mesh-free kernel particle functions. Single-walled carbon nanotubes (SWCNTs) are selected as reinforcement and effective material properties of FG-CNTRC plates are assumed to be graded through the thickness direction and are estimated through an equivalent continuum model based on the Eshelby–Mori–Tanaka approach. For eliminating shear locking for a very thin plate, a stabilized conforming nodal integration scheme is employed to evaluate the system bending stiffness, and the membrane as well as shear terms are calculated by the direct nodal integration method. Numerical simulations are carried out to investigate effects of various parameters on nonlinear behaviors of FG-CNTRC plates and results for uniformly distributed (UD) CNTRC plates are provided for comparison. Numerical results indicate that carbon nanotube content by volume, plate width-to-thickness ratio, plate aspect ratio and boundary condition have pronounced effects on the nonlinear response of CNTRC plates.

© 2012 Elsevier B.V. All rights reserved.

## 1. Introduction

In recent years, carbon nanotubes (CNTs) have attracted much attention from researchers. Owing to their remarkable mechanical, electrical and thermal properties, CNTs have been widely accepted as a potential constituent of reinforcement and multi-functional element for nanocomposites [1–3]. Extant research [4] has demonstrated that addition of 1phr (part per hundred parts of resin) of multi-walled CNTs in a styrene-butadiene copolymer results in a 45% increase in modulus and a 70% increase in tensile length. Qian et al. [5] investigated load transfer and deformation mechanisms in carbon nanotube-polystyrene composites and found that addition of only 1 wt% nanotubes resulted in 36–42% and 25% increase in elastic modulus as well as break stress. Pötschke et al. [6] examined rheological behavior of compression molded mixtures of polycarbonate and carbon nanotubes containing nanotube concentrations of 0.5 wt% to 15 wt% using oscillatory rheometry at 260°C. They discovered that 2 wt% nanotubes caused an obvious change in electrical resistivity and complex viscosity. Therefore, the introduction of CNTs into a polymer matrix may greatly im-

prove mechanical, electrical and thermal properties of the resulting nanocomposites.

Since the load transfer between the nanotube and the matrix is less than perfect, several micromechanical models have been developed to predict properties of CNT-reinforced nanocomposites. Fidelus et al. [7] examined thermo-mechanical properties of epoxy-based nanocomposites with low weight fractions (from 0.01 to 0.5 wt%) of randomly oriented single- and multi-walled carbon nanotubes with a rule-of-mixture type prediction of the modulus. Based on the rule of mixture, Anumandla and Gibson [8] presented a comprehensive closed form micromechanics model for estimating the elastic modulus of nanotube-reinforced composites. Han and Elliot [9] presented classical molecular dynamics (MD) simulations of model polymer/CNT composites constructed by embedding a single wall (10, 10) CNT into two different amorphous polymer matrices. The results showed that the MD results matched very well with results obtained from the rule of mixture. For most of the equivalent continuum approaches, Eshelby theory [10,11] played a crucial role in modeling nanocomposites. Based on Eshelby–Mori–Tanaka approach, Formica and Lacarbonara [12] employed a continuum model for carbon nanotube-based composites as well as Shi et al. [13] investigated the effect of nanotube waviness and agglomeration on elastic properties of CNTRCs. Li et al. [14] studied reinforcing mechanisms of SWCNT-reinforced

\* Corresponding author at: Department of Civil and Architectural Engineering, City University of Hong Kong, Kowloon, Hong Kong.

E-mail address: [kmliew@cityu.edu.hk](mailto:kmliew@cityu.edu.hk) (K.M. Liew).

epoxy composites by several micromechanics models and found that the modeling results obtained from both Halpin–Tsai and Mori–Tanaka models were in good agreement with the experimental results.

Functionally graded materials (FGMs) in which material properties spatially vary according to a certain non-uniform distribution of one of the constituents offer great potential for use in various engineering applications. Numerous studies have been carried out to examine usage of FGMs in a wide range of fields since the concept of FGMs was first proposed in 1984 [15,16]. Stimulated by the concept of functionally graded materials, the pattern of the functionally graded distribution of reinforcement has been successfully applied for CNTRCs. Zhu et al. [17] carried out bending and free vibration analyses of various types of functionally graded CNTRC plates using the finite element method (FEM). Using a two-step perturbation technique, Shen [18] presented a nonlinear bending analysis of functionally graded carbon nanotube-reinforced composite (FG-CNTRC) plates in thermal environments. Ke et al. [19] investigated nonlinear free vibration responses of functionally graded nanocomposite beams reinforced by SWCNTs. Based on the Eshelby–Mori–Tanaka approach, natural frequency characteristics of a continuously graded CNTs-reinforced cylindrical panels were considered by Aragh et al. [20] and vibrational properties of CNTRCs were also studied by Formica et al. [21]. Mehrabadi [22] investigated mechanical buckling of functionally graded nanocomposites rectangular plates reinforced by aligned and straight SWCNTs subjected to uniaxial and biaxial in-plane loadings, in which the effective material properties of nanocomposites were estimated by either the Eshelby–Mori–Tanaka approach or the extended rule of mixture. For postbuckling analyses, CNTRC cylindrical shells subject to axial compression and lateral pressure in thermal environments were investigated by Shen [23,24] as well as a similar analysis of functionally graded nanocomposite plates subjected to in-plane temperature variation was also presented by Shen and Zhang [25].

In the present work, a nonlinear bending analysis of FG-CNTRC plates is presented using the element-free *kp*-Ritz method, which has already been successfully applied in many fields [26–29]. The nonlinear bending formulation is based on the first-order shear deformation plate theory and the Von Kármán assumption accounting for transverse shear strains, rotary inertia and moderate rotations. Two kinds of CNTRC plates, namely, UD and FG distributions of the reinforcement are considered. The material properties of FG-CNTRCs are assumed to be graded in the thickness direction and are estimated through an equivalent continuum model based on the Eshelby–Mori–Tanaka approach. In the present meshfree method, plate bending stiffness is calculated using a stabilized conforming nodal integration approach while the shear and membrane stiffness are evaluated using a direct nodal integration method to avoid shear locking for very thin plates. A combination of the arc-length iterative algorithm and the modified Newton–Raphson method is employed to obtain nonlinear response of FG-CNTRC plates. The current formulation is verified by several studies that compared the present results with solutions reported in the literature. Detailed parametric studies are also carried out to investigate the effects of CNT content by volume, plate width-to-thickness ratio, plate aspect ratio and boundary condition on the nonlinear responses in detail.

## 2. Carbon nanotube-reinforced composites

As shown in Fig. 1, four types of CNTRC plates with length *a*, width *b* and thickness *h* are considered. The CNTs are assumed uniaxially aligned, that is, UD represents uniformly distributed and FG-V, FG-O and FG-X denote the other three types of function-

ally graded distributions of CNTs. According to distributions of uniaxially aligned SWCNTs, CNT content by volume  $V_{CNT}$  are expressed as [17]

$$V_{CNT}(z) = \begin{cases} V_{CNT}^* & \text{(UD),} \\ (1 + \frac{2z}{h})V_{CNT}^* & \text{(FG-V),} \\ 2(1 - \frac{2|z|}{h})V_{CNT}^* & \text{(FG-O),} \\ 2(\frac{2|z|}{h})V_{CNT}^* & \text{(FG-X),} \end{cases} \quad (1)$$

where UD represents the uniform distribution. For the type of FG-V, the top surface of the CNTRC plate is CNT-rich. In FG-O, the mid-plane of the CNTRC plate is CNT-rich and in case of FG-X, both top and bottom surfaces of the CNTRC plate are CNT-rich, and

$$V_{CNT}^* = \frac{w_{CNT}}{w_{CNT} + (\rho_{CNT}^{CNT}/\rho^m) - (\rho_{CNT}^{CNT}/\rho^m)w_{CNT}}, \quad (2)$$

in which  $w_{CNT}$  is the mass fraction of CNTs and  $\rho^m$  and  $\rho^{CNT}$  are densities of the matrix and CNTs, respectively. The overall CNT content by volume of UD-CNTRC plate and those of the other three types of FG-CNTRC plates are the same, which means the four types CNTRC plates have the same mass and volume of CNTs. In this paper, an equivalent continuum model based on the Eshelby–Mori–Tanaka approach is employed to predict properties of carbon nanotube-reinforced nanocomposites [10,11,30]. For two-phase composites, effective elastic module tensor  $\mathbf{L}$  of CNTRCs can be expressed as follows, according to Benveniste’s revision [31]:

$$\mathbf{L} = \mathbf{L}_m + V_{CNT} \langle (\mathbf{L}_{CNT} - \mathbf{L}_m) \cdot \mathbf{A} \rangle \cdot [V_m \mathbf{I} + V_{CNT} \langle \mathbf{A} \rangle]^{-1}, \quad (3)$$

where  $\mathbf{L}_m$  and  $\mathbf{L}_{CNT}$  are stiffness tensors of the matrix and CNT, respectively.  $\mathbf{I}$  is the fourth-order unit tensor. The angle brackets represent an average over all possible orientation of the inclusions.  $\mathbf{A}$  is the dilute mechanical strain concentration tensor, and is written as

$$\mathbf{A} = [\mathbf{I} + \mathbf{S} \cdot \mathbf{L}_m^{-1} \cdot (\mathbf{L}_{CNT} - \mathbf{L}_m)]^{-1}, \quad (4)$$

where  $\mathbf{S}$  is the fourth-order Eshelby tensor [11] and is well defined for cylindrical inclusions by Mura [32].

## 3. Theoretical formulations

### 3.1. Total potential energy functional

The nonlinear bending formulations of CNTRC plate are derived here from the Ritz method. The displacement field of the first-order shear deformation theory (FSDT) is of the form [33]

$$u(x, y, z) = u_0(x, y) + z\phi_x(x, y), \quad (5)$$

$$v(x, y, z) = v_0(x, y) + z\phi_y(x, y), \quad (6)$$

$$w(x, y, z) = w_0(x, y), \quad (7)$$

where *u*, *v* and *w* are displacements of a point in question within the CNTRC plate along the *x*, *y* and *z* directions, respectively, and  $u_0$ ,  $v_0$  and  $w_0$  represent the displacements of a point on the plate  $z = 0$ . It is worth to note that

$$\phi_x = \frac{\partial u}{\partial z}, \quad \phi_y = \frac{\partial v}{\partial z}, \quad (8)$$

which indicate that  $\phi_x$  and  $\phi_y$  are transverse normal rotations about positive *y* and negative *x* axes, respectively. Based on the above displacement field, the strain components can be expressed by

$$\begin{Bmatrix} \epsilon_{xx} \\ \epsilon_{yy} \\ \gamma_{xy} \end{Bmatrix} = \boldsymbol{\epsilon}_0 + z\boldsymbol{\kappa}, \quad \begin{Bmatrix} \gamma_{yz} \\ \gamma_{xz} \end{Bmatrix} = \boldsymbol{\gamma}_0, \quad (9)$$

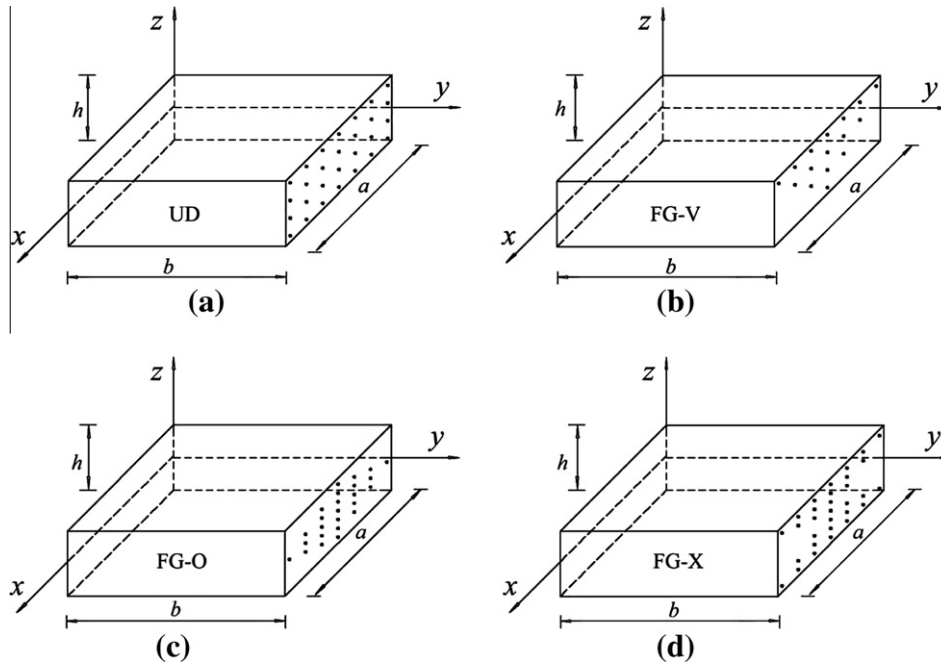


Fig. 1. Configurations of carbon nanotube reinforced composite plates: (a) UD CNTRC plate, (b) FG-V CNTRC plate, (c) FG-O CNTRC plate, (d) FG-X CNTRC plate.

where

$$\boldsymbol{\varepsilon}_0 = \boldsymbol{\varepsilon}_{0L} + \boldsymbol{\varepsilon}_{0N}, \tag{10}$$

$$\boldsymbol{\kappa} = \begin{Bmatrix} \frac{\partial \phi_x}{\partial x} \\ \frac{\partial \phi_y}{\partial y} \\ \frac{\partial \phi_x}{\partial y} + \frac{\partial \phi_y}{\partial x} \end{Bmatrix}, \quad \boldsymbol{\gamma}_0 = \begin{Bmatrix} \phi_y + \frac{\partial w_0}{\partial y} \\ \phi_x + \frac{\partial w_0}{\partial x} \end{Bmatrix}, \tag{11}$$

where the linear and nonlinear terms are expressed as:

$$\boldsymbol{\varepsilon}_{0L} = \begin{Bmatrix} \frac{\partial u_0}{\partial x} \\ \frac{\partial v_0}{\partial y} \\ \frac{\partial u_0}{\partial y} + \frac{\partial v_0}{\partial x} \end{Bmatrix}, \quad \boldsymbol{\varepsilon}_{0N} = \begin{Bmatrix} \frac{1}{2} \left( \frac{\partial w_0}{\partial x} \right)^2 \\ \frac{1}{2} \left( \frac{\partial w_0}{\partial y} \right)^2 \\ \frac{\partial w_0}{\partial x} \frac{\partial w_0}{\partial y} \end{Bmatrix}. \tag{12}$$

Then, the constitutive relations are given by

$$\begin{Bmatrix} \sigma_{xx} \\ \sigma_{yy} \\ \sigma_{xy} \\ \sigma_{yz} \\ \sigma_{xz} \end{Bmatrix} = \begin{bmatrix} Q_{11} & Q_{12} & 0 & 0 & 0 \\ Q_{12} & Q_{22} & 0 & 0 & 0 \\ 0 & 0 & Q_{66} & 0 & 0 \\ 0 & 0 & 0 & Q_{44} & 0 \\ 0 & 0 & 0 & 0 & Q_{55} \end{bmatrix} \left( \begin{Bmatrix} \varepsilon_{xx} \\ \varepsilon_{yy} \\ \gamma_{xy} \\ \gamma_{yz} \\ \gamma_{xz} \end{Bmatrix} - \begin{Bmatrix} \alpha_{11} \\ \alpha_{22} \\ 0 \\ 0 \\ 0 \end{Bmatrix} \Delta T \right), \tag{13}$$

where

$$Q_{11} = \frac{E_{11}}{1 - \nu_{12}\nu_{21}}, \quad Q_{22} = \frac{E_{22}}{1 - \nu_{12}\nu_{21}}, \quad Q_{12} = \frac{\nu_{21}E_{11}}{1 - \nu_{12}\nu_{21}}, \\ Q_{66} = G_{12}, \quad Q_{44} = G_{23}, \quad Q_{55} = G_{13}, \tag{14}$$

and  $\alpha_{11}$  and  $\alpha_{22}$  are thermal expansion coefficients in  $x$  and  $y$  directions, respectively, and  $\Delta T$  is the temperature change from a reference stress free state.

The relationship between the resultant stresses and the strains can be written as

$$\begin{Bmatrix} \mathbf{N} \\ \mathbf{M} \\ \mathbf{Q}_s \end{Bmatrix} = \begin{bmatrix} \mathbf{A} & \mathbf{B} & \mathbf{0} \\ \mathbf{B} & \mathbf{D} & \mathbf{0} \\ \mathbf{0} & \mathbf{0} & \mathbf{A}^s \end{bmatrix} \begin{Bmatrix} \boldsymbol{\varepsilon}_0 \\ \boldsymbol{\kappa} \\ \boldsymbol{\gamma}_0 \end{Bmatrix} - \begin{Bmatrix} \mathbf{N}^T \\ \mathbf{M}^T \\ \mathbf{0} \end{Bmatrix}, \tag{15}$$

where the total in-plane force resultants, total moment resultants, transverse shear force resultants and thermal stress resultants are defined as

$$\mathbf{N} = \begin{Bmatrix} N_{xx} \\ N_{yy} \\ N_{xy} \end{Bmatrix} = \int_{-h/2}^{h/2} \begin{Bmatrix} \sigma_{xx} \\ \sigma_{yy} \\ \sigma_{xy} \end{Bmatrix} dz, \tag{16}$$

$$\mathbf{M} = \begin{Bmatrix} M_{xx} \\ M_{yy} \\ M_{xy} \end{Bmatrix} = \int_{-h/2}^{h/2} \begin{Bmatrix} \sigma_{xx} \\ \sigma_{yy} \\ \sigma_{xy} \end{Bmatrix} z dz, \tag{17}$$

$$\mathbf{Q}_s = \begin{Bmatrix} Q_y \\ Q_x \end{Bmatrix} = \int_{-h/2}^{h/2} \begin{Bmatrix} \sigma_{yz} \\ \sigma_{xz} \end{Bmatrix} dz, \tag{18}$$

$$\mathbf{N}^T = \int_{-h/2}^{h/2} [\alpha_{11} \quad \alpha_{22} \quad 0] (Q_{11} + Q_{12}) \Delta T dz, \tag{19}$$

$$\mathbf{M}^T = \int_{-h/2}^{h/2} [\alpha_{11} \quad \alpha_{22} \quad 0] (Q_{11} + Q_{12}) \Delta T z dz. \tag{20}$$

The stiffness matrixes  $\mathbf{A}$ ,  $\mathbf{B}$ ,  $\mathbf{D}$  and  $\mathbf{A}^s$  are given as

$$(A_{ij}, B_{ij}, D_{ij}) = \int_{-h/2}^{h/2} Q_{ij}(1, z, z^2) dz, \quad A_{ij}^s = K \int_{-h/2}^{h/2} Q_{ij} dz, \tag{21}$$

where  $A_{ij}$ ,  $B_{ij}$  and  $D_{ij}$  are defined for  $ij = 1, 2, 6$  and  $ij = 4, 5$  in  $A_{ij}^s$ . For isotropic materials, the transverse shear correction coefficient  $K$  is taken to be  $5/6$ , and is suggested to be  $K = 5/(6 - (\nu_1 V_1 + \nu_2 V_2))$  for functionally graded materials by Efraim and Eisenberger [34].

The strain energy of the CNTRC plate is expressed as

$$U_\varepsilon = \frac{1}{2} \int_\Omega \boldsymbol{\varepsilon}^T \mathbf{S} \boldsymbol{\varepsilon} d\Omega, \tag{22}$$

where

$$\boldsymbol{\varepsilon} = \begin{Bmatrix} \boldsymbol{\varepsilon}_0 \\ \boldsymbol{\kappa} \\ \boldsymbol{\gamma}_0 \end{Bmatrix}, \quad \mathbf{S} = \begin{bmatrix} \mathbf{A} & \mathbf{B} & \mathbf{0} \\ \mathbf{B} & \mathbf{D} & \mathbf{0} \\ \mathbf{0} & \mathbf{0} & \mathbf{A}^s \end{bmatrix}. \tag{23}$$

The external work is given by

$$W_e = \int_{\Omega} \mathbf{u}^T \bar{\mathbf{f}} d\Omega + \int_{\Gamma} \mathbf{u}^T \bar{\mathbf{t}} d\Gamma, \quad (24)$$

where  $\bar{\mathbf{f}}$  represents the external load and  $\bar{\mathbf{t}}$  is the prescribed traction on the natural boundary.  $\mathbf{u}$  is the displacement vector.

Thus the total potential energy functional of the plate can be expressed as

$$\Pi_s = U_e - W_e. \quad (25)$$

### 3.2. Discrete system equations

In the present work, CNTRC plates are discretized by a group of nodes  $\mathbf{x}_I, I = 1, \dots, NP$ . The displacement field of CNTRC plates can be expressed according to the reproducing kernel particle method

$$\hat{\mathbf{u}} = \sum_{I=1}^{NP} \psi_I(\mathbf{x}) \mathbf{u}_I, \quad (26)$$

where  $\mathbf{u}_I$  is and displacement associated with node  $I$ .  $\psi_I(\mathbf{x})$  is the two-dimensional shape function defined as [35,36]:

$$\psi_I(\mathbf{x}) = C(\mathbf{x}; \mathbf{x} - \mathbf{x}_I) \Phi_a(\mathbf{x} - \mathbf{x}_I), \quad (27)$$

where  $\Phi_a(\mathbf{x} - \mathbf{x}_I)$  is the kernel function. Correction function  $C(\mathbf{x}; \mathbf{x} - \mathbf{x}_I)$  is constructed as a linear combination of polynomial basis functions to satisfy reproducing conditions

$$C(\mathbf{x}; \mathbf{x} - \mathbf{x}_I) = \mathbf{H}^T(\mathbf{x} - \mathbf{x}_I) \mathbf{b}(\mathbf{x}), \quad (28)$$

where

$$\mathbf{b}(\mathbf{x}) = [b_0(x, y), b_1(x, y), b_2(x, y), b_3(x, y), b_4(x, y), b_5(x, y)]^T, \quad (29)$$

$$\mathbf{H}^T(\mathbf{x} - \mathbf{x}_I) = [1, x - x_I, y - y_I, (x - x_I)(y - y_I), (x - x_I)^2, (y - y_I)^2], \quad (30)$$

where  $\mathbf{H}$  is a quadratic basis vector.  $\mathbf{b}(\mathbf{x})$  is a coefficient function of  $x$  and  $y$  to be determined.

Now, the shape function can be written as

$$\psi_I(\mathbf{x}) = \mathbf{b}^T(\mathbf{x}) \mathbf{H}(\mathbf{x} - \mathbf{x}_I) \Phi_a(\mathbf{x} - \mathbf{x}_I), \quad (31)$$

The coefficient  $\mathbf{b}(\mathbf{x})$  can be obtained by substituting Eq. (28) into reproduction conditions

$$\sum_{I=1}^{NP} \psi_I(\mathbf{x}) x_I^p y_I^q = x^p y^q \quad \text{for } p + q = 0, 1, 2. \quad (32)$$

$$\mathbf{b}(\mathbf{x}) = \mathbf{M}^{-1}(\mathbf{x}) \mathbf{H}(\mathbf{0}), \quad (33)$$

where

$$\mathbf{M}(\mathbf{x}) = \sum_{I=1}^{NP} \mathbf{H}(\mathbf{x} - \mathbf{x}_I) \mathbf{H}^T(\mathbf{x} - \mathbf{x}_I) \Phi_a(\mathbf{x} - \mathbf{x}_I), \quad (34)$$

$$\mathbf{H}(\mathbf{0}) = [1, 0, 0, 0, 0, 0]^T, \quad (35)$$

The two-dimensional kernel function  $\Phi_a(\mathbf{x} - \mathbf{x}_I)$  is defined as

$$\Phi_a(\mathbf{x} - \mathbf{x}_I) = \Phi_a(\mathbf{x}) \cdot \Phi_a(y), \quad (36)$$

where

$$\Phi_a(x) = \varphi\left(\frac{x - x_I}{a}\right). \quad (37)$$

The cubic spline function is employed as the weight function  $\varphi(x)$

$$\varphi_2(z_I) = \begin{cases} \frac{2}{3} - 4z_I^2 + 4z_I^3 & \text{for } 0 \leq |z_I| \leq \frac{1}{2}, \\ \frac{4}{3} - 4z_I + 4z_I^2 - \frac{4}{3}z_I^3 & \text{for } \frac{1}{2} < |z_I| \leq 1, \\ 0 & \text{otherwise,} \end{cases} \quad (38)$$

where  $z_I = \frac{x - x_I}{d_I}$ ,  $d_I$  is the size of the support of node  $I$ , calculated by

$$d_I = d_{\max} c_I, \quad (39)$$

in which  $d_{\max}$  is a scaling factor ranging from 2.0 to 4.0, and distance  $c_I$  is chosen by searching a sufficient number of nodes to avoid the singularity of the matrix  $\mathbf{M}$ .

The shape function can be expressed as

$$\psi_I(\mathbf{x}) = \mathbf{H}^T(\mathbf{0}) \mathbf{M}^{-1}(\mathbf{x}) \mathbf{H}(\mathbf{x} - \mathbf{x}_I) \Phi_a(\mathbf{x} - \mathbf{x}_I). \quad (40)$$

As the shape function  $\psi_I(\mathbf{x})$  does not possess Kronecker delta property, the essential boundary conditions cannot be directly imposed. Several methods, such as the transformation method [35], Lagrange multipliers and the penalty method can be applied to enforce the essential boundary conditions. In this paper, the transformation method is employed to impose the essential boundary conditions. For the transformation approach, a transformation matrix is introduced to the reconstruction of the present shape functions that possess Kronecker delta property. Then direct treatment of boundary conditions is allowed and hence the kinematically admissible test and trial functions can be formed.

Based on the displacements defined in Eq. (26), the ‘generalized’ displacement  $\tilde{\mathbf{u}}$  is constructed as

$$\tilde{\mathbf{u}}_j = \sum_{I=1}^{NP} \psi_I(x_j) \mathbf{u}_I = \sum_{K=1}^{NP} L_{jK} \mathbf{u}_K, \quad (41)$$

where  $\tilde{\mathbf{u}}_j = \hat{\mathbf{u}}(x_j)$  is the nodal value at  $x_j$  and  $L_{jK} = \psi_I(x_j)$ .

Then we can obtain

$$\mathbf{u}_I = \sum_{K=1}^{NP} L_{IK}^{-T} \tilde{\mathbf{u}}_K. \quad (42)$$

Substituting Eq. (42) into Eq. (41) leads to

$$\hat{\mathbf{u}}_I = \sum_{I=1}^{NP} \psi_I(x) \mathbf{u}_I = \sum_{I=1}^{NP} \sum_{K=1}^{NP} \psi_I(x) L_{IK}^{-T} \tilde{\mathbf{u}}_K = \sum_{K=1}^{NP} \hat{\psi}_K(x) \tilde{\mathbf{u}}_K, \quad (43)$$

where

$$\hat{\psi}_K(x) = \sum_{I=1}^{NP} L_{KI}^{-T} \psi_I(x). \quad (44)$$

Note that

$$\hat{\psi}_I(x_j) = \sum_{I=1}^{NP} L_{IK}^{-T} \psi_K(x_j) = \sum_{I=1}^{NP} L_{IK}^{-T} L_{Kj} = \delta_{Ij}. \quad (45)$$

Therefore, the reconstruction shape function possesses Kronecker delta property.

Substituting Eqs. (26) into (22), the strain energy can be written as

$$\begin{aligned} U_e &= U_L + U_N \\ &= \frac{1}{2} \int_{\Omega} (\boldsymbol{\varepsilon}_{0L}^T \mathbf{A} \boldsymbol{\varepsilon}_{0L} + \boldsymbol{\varepsilon}_{0L}^T \mathbf{B} \boldsymbol{\kappa} + \boldsymbol{\kappa}^T \mathbf{B} \boldsymbol{\varepsilon}_{0L} + \boldsymbol{\kappa}^T \mathbf{D} \boldsymbol{\kappa} + \boldsymbol{\gamma}^T \mathbf{A}^s \boldsymbol{\gamma}) dx dy \\ &\quad + \int_{\Omega} (\boldsymbol{\varepsilon}_{0L}^T \mathbf{A} \boldsymbol{\varepsilon}_{0N} + \boldsymbol{\varepsilon}_{0N}^T \mathbf{A} \boldsymbol{\varepsilon}_{0L} + \boldsymbol{\varepsilon}_{0N}^T \mathbf{B} \boldsymbol{\varepsilon}_{0N} + \boldsymbol{\kappa}^T \mathbf{D} \boldsymbol{\varepsilon}_{0N} + \boldsymbol{\varepsilon}_{0N}^T \mathbf{A} \boldsymbol{\varepsilon}_{0N}) dx dy. \end{aligned} \quad (46)$$

Taking the variation of the total potential energy functional, it yields the nonlinear bending equilibrium equation

$$\mathbf{K}_s(\mathbf{u}) \mathbf{u} = \mathbf{F}, \quad (47)$$

where the nonlinear stiffness matrix  $\mathbf{K}_s(\mathbf{u})$  is decomposed into two terms

$$\mathbf{K}_s(\mathbf{u}) = \mathbf{K}^L + \mathbf{K}^N(\mathbf{u}), \quad (48)$$

in which  $\mathbf{K}^L$  and  $\mathbf{K}^N(\mathbf{u})$  represent the linear and nonlinear parts of the stiffness matrix, respectively, and are calculated by

$$\mathbf{K}^L = \mathbf{K}^b + \mathbf{K}^m + \mathbf{K}^s + \mathbf{K}^t, \quad (49)$$

$$\mathbf{K}_{ij}^b = \int_{\Omega} \mathbf{B}_i^{bT} \mathbf{D} \mathbf{B}_j^b d\Omega, \quad (50)$$

$$\mathbf{K}_{ij}^m = \int_{\Omega} \mathbf{B}_i^{mT} \mathbf{A} \mathbf{B}_j^m d\Omega + \int_{\Omega} \mathbf{B}_i^{mT} \bar{\mathbf{B}} \mathbf{B}_j^b d\Omega + \int_{\Omega} \mathbf{B}_i^{bT} \bar{\mathbf{B}} \mathbf{B}_j^m d\Omega, \quad (51)$$

$$\mathbf{K}_{ij}^s = \int_{\Omega} \mathbf{B}_i^{sT} \mathbf{A}^s \mathbf{B}_j^s d\Omega, \quad (52)$$

$$\mathbf{K}^t = \int_{\Omega} \bar{\mathbf{G}}_i^T \bar{\mathbf{N}} \mathbf{G}_j d\Omega, \quad (53)$$

$$\mathbf{F}_i = \int_{\Omega} \psi_i \bar{\mathbf{f}} d\Omega + \int_{\Gamma} \psi_i \bar{\mathbf{t}} d\Gamma + \int_{\Omega} \begin{bmatrix} \mathbf{B}_i^{mT} & \mathbf{B}_i^{bT} \\ \mathbf{M}^T \end{bmatrix} \begin{bmatrix} \mathbf{N}^T \\ \mathbf{M}^T \end{bmatrix} d\Omega, \quad (54)$$

$$\mathbf{K}_{ij}^N = \int_{\Omega} \left( \frac{1}{2} \mathbf{B}_i^{T} \mathbf{S} \mathbf{B}_j^N + \mathbf{B}_i^{N^T} \mathbf{S} \mathbf{B}_j^L + \frac{1}{2} \mathbf{B}_i^{N^T} \mathbf{S} \mathbf{B}_j^N \right) d\Omega, \quad (55)$$

$$\mathbf{B}_i^L = \begin{bmatrix} \mathbf{B}_i^m \\ \mathbf{B}_i^b \\ \mathbf{B}_i^s \end{bmatrix}, \quad \mathbf{B}_i^N = \bar{\mathbf{H}} \mathbf{G}. \quad (56)$$

Compared with the Gauss integration, the stabilized nodal integration and direct nodal integration may reduce the high computational cost and eliminate the errors due to the mismatch between the quadrature cells and the shape function supports [37]. Then the bending stiffness matrices in Eq. (50) are evaluated via the stabilized nodal integration [38] while the shear and membrane terms in Eqs. (51)–(55) are calculated using direct nodal integration [39] instead of the Gauss integration which are commonly used in mesh-free methods. Approximations of Eqs. (50)–(55) are given as follows:

$$\mathbf{K}_{ij}^b = \sum_{L=1}^{NP} \tilde{\mathbf{B}}_i^{bT}(\mathbf{x}_L) \mathbf{D} \tilde{\mathbf{B}}_j^b(\mathbf{x}_L) A_L, \quad (57)$$

$$\mathbf{K}_{ij}^m = \sum_{L=1}^{NP} \left[ \mathbf{B}_i^{mT}(\mathbf{x}_L) \mathbf{A} \mathbf{B}_j^m(\mathbf{x}_L) + \mathbf{B}_i^{mT}(\mathbf{x}_L) \bar{\mathbf{B}} \mathbf{B}_j^b(\mathbf{x}_L) + \mathbf{B}_i^{bT}(\mathbf{x}_L) \bar{\mathbf{B}} \mathbf{B}_j^m(\mathbf{x}_L) \right] A_L, \quad (58)$$

$$\mathbf{K}_{ij}^s = \sum_{L=1}^{NP} \mathbf{B}_i^{sT}(\mathbf{x}_L) \mathbf{A}^s \mathbf{B}_j^s(\mathbf{x}_L) A_L, \quad (59)$$

$$\mathbf{K}^t = \sum_{L=1}^{NP} \bar{\mathbf{G}}_i^T(\mathbf{x}_L) \bar{\mathbf{N}} \mathbf{G}_j(\mathbf{x}_L) A_L, \quad (60)$$

$$\mathbf{K}_{ij}^N = \sum_{L=1}^{NP} \left[ \frac{1}{2} \mathbf{B}_i^{T}(\mathbf{x}_L) \mathbf{S} \mathbf{B}_j^N(\mathbf{x}_L) + \mathbf{B}_i^{N^T}(\mathbf{x}_L) \mathbf{S} \mathbf{B}_j^L(\mathbf{x}_L) + \frac{1}{2} \mathbf{B}_i^{N^T}(\mathbf{x}_L) \mathbf{S} \mathbf{B}_j^N(\mathbf{x}_L) \right] A_L, \quad (61)$$

$$\mathbf{F}_i = \sum_{L=1}^{NP} \psi_i(\mathbf{x}_L) \bar{\mathbf{f}}(\mathbf{x}_L) A_L + \sum_{L=1}^{NPb} \psi_i(\mathbf{x}_L) \bar{\mathbf{t}}(\mathbf{x}_L) s_L + \sum_{L=1}^{NP} \begin{bmatrix} \mathbf{B}_i^{mT}(\mathbf{x}_L) & \mathbf{B}_i^{bT}(\mathbf{x}_L) \\ \mathbf{M}^T \end{bmatrix} \begin{bmatrix} \mathbf{N}^T \\ \mathbf{M}^T \end{bmatrix} A_L, \quad (62)$$

where  $\mathbf{x}_L$  and  $A_L$  indicate the nodal coordinate and representative area, respectively, as well as  $NP$  and  $s_L$  represent the number of nodes on the natural boundary and the weights associated with the boundary point, respectively. Here matrices  $\tilde{\mathbf{B}}_i^b(\mathbf{x}_L)$ ,  $\mathbf{B}_i^b(\mathbf{x}_L)$ ,  $\mathbf{B}_i^m(\mathbf{x}_L)$ ,  $\mathbf{B}_i^s(\mathbf{x}_L)$ ,  $\bar{\mathbf{G}}(\mathbf{x}_L)$  and  $\bar{\mathbf{N}}$  are calculated by:

$$\tilde{\mathbf{B}}_i^b(\mathbf{x}_L) = \begin{bmatrix} 0 & 0 & 0 & \tilde{b}_{ix}(\mathbf{x}_L) & 0 \\ 0 & 0 & 0 & 0 & \tilde{b}_{iy}(\mathbf{x}_L) \\ 0 & 0 & 0 & \tilde{b}_{iy}(\mathbf{x}_L) & \tilde{b}_{ix}(\mathbf{x}_L) \end{bmatrix}, \quad (63)$$

$$\begin{aligned} \tilde{b}_{ix}(\mathbf{x}_L) &= \frac{1}{A_L} \int_{\Gamma_L} \psi_i(\mathbf{x}_L) n_x(\mathbf{x}_L) d\Gamma, & \tilde{b}_{iy}(\mathbf{x}_L) \\ &= \frac{1}{A_L} \int_{\Gamma_L} \psi_i(\mathbf{x}_L) n_y(\mathbf{x}_L) d\Gamma, \end{aligned} \quad (64)$$

$$\mathbf{B}_i^b(\mathbf{x}_L) = \begin{bmatrix} 0 & 0 & 0 & \frac{\partial \psi_i(\mathbf{x}_L)}{\partial x} & 0 \\ 0 & 0 & 0 & 0 & \frac{\partial \psi_i(\mathbf{x}_L)}{\partial y} \\ 0 & 0 & 0 & \frac{\partial \psi_i(\mathbf{x}_L)}{\partial y} & \frac{\partial \psi_i(\mathbf{x}_L)}{\partial x} \end{bmatrix}, \quad (65)$$

$$\mathbf{B}_i^m(\mathbf{x}_L) = \begin{bmatrix} \frac{\partial \psi_i(\mathbf{x}_L)}{\partial x} & 0 & 0 & 0 & 0 \\ 0 & \frac{\partial \psi_i(\mathbf{x}_L)}{\partial y} & 0 & 0 & 0 \\ \frac{\partial \psi_i(\mathbf{x}_L)}{\partial y} & \frac{\partial \psi_i(\mathbf{x}_L)}{\partial x} & 0 & 0 & 0 \end{bmatrix}, \quad (66)$$

$$\mathbf{B}_i^s(\mathbf{x}_L) = \begin{bmatrix} 0 & 0 & \frac{\partial \psi_i(\mathbf{x}_L)}{\partial x} & \psi_i(\mathbf{x}_L) & 0 \\ 0 & 0 & \frac{\partial \psi_i(\mathbf{x}_L)}{\partial y} & 0 & \psi_i(\mathbf{x}_L) \end{bmatrix}, \quad (67)$$

$$\bar{\mathbf{H}} = \begin{bmatrix} \frac{\partial w}{\partial x} & 0 & \frac{\partial w}{\partial y} & 0 & 0 \\ 0 & \frac{\partial w}{\partial y} & \frac{\partial w}{\partial x} & 0 & 0 \end{bmatrix}^T, \quad (68)$$

$$\bar{\mathbf{G}}(\mathbf{x}_L) = \begin{bmatrix} 0 & 0 & \frac{\partial \psi_i(\mathbf{x}_L)}{\partial x} & 0 & 0 \\ 0 & 0 & \frac{\partial \psi_i(\mathbf{x}_L)}{\partial y} & 0 & 0 \end{bmatrix}, \quad \bar{\mathbf{N}} = \begin{bmatrix} N_{xx} & 0 \\ 0 & N_{yy} \end{bmatrix}. \quad (69)$$

A brief flowchart of the proposed method is shown in Fig. 2, in which a combination of the arc-length iterative algorithm and the modified Newton–Raphson method is employed to obtain nonlinear responses of FG-CNTRC plates.

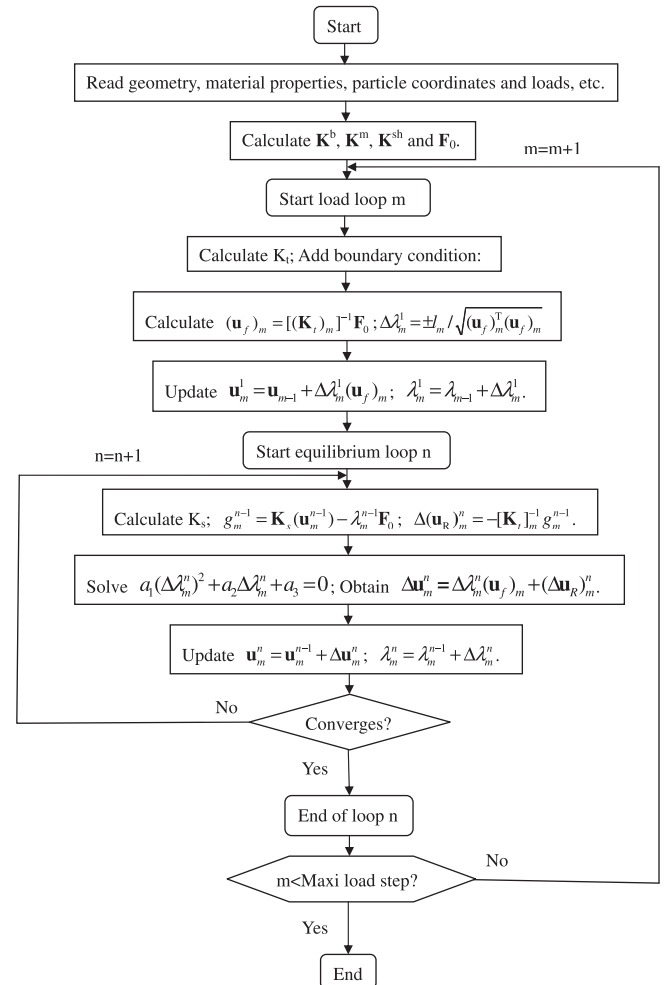


Fig. 2. The flowchart of the proposed method for nonlinear analysis of CNTRC plates.

4. Numerical results

This section first reports the outcome of nonlinear analyses of isotropic, orthotropic and functionally graded alumina/aluminum plates for comparison and verification of accuracy as well as effectiveness of the present method. Then detailed parametric studies are presented to illustrate the linear and nonlinear responses of CNTRC plates. Poly((m-phenylenevinylene)-co-[(2,5-dioctoxy-p-phenylene) vinylene]), referred as PmPV, is selected as the matrix with isotropic material properties  $\nu_m = 0.34$  and  $E_m = (3.51 - 0.0047T)$  GPa, where  $T = T_0 + \Delta T$  and  $T_0 = 300$  K (room temperature). As material properties of SWCNTs are charity-, size- and temperature-dependent [40–43], typical values are taken from analytical results of Popov et al. [44]. In this paper, properties of the matrix and CNTs are given as at temperature  $T = 300$  K (room temperature) unless otherwise specified. For the present element-free method, a scaling factor of 2.2 that represents the size of the support is used in construction of shape functions and a regular nodal distribution  $15 \times 15$  is chosen, following convergence studies.

4.1. Nonlinear analysis of isotropic, orthotropic and functionally graded alumina/aluminum plates

To verify the present formulation, several comparisons are carried out. A convergence study is carried out first for nonlinear bending analysis of simply supported square isotropic plate ( $\nu = 0.316$ ) subjected to a uniform distributed transverse load in terms of the number of nodes. The non-dimensional load–deflection curves are shown in Fig. 3. It can be seen that the result obtained by the present element-free method with  $15 \times 15$  nodes agrees well with solution of Shen [45] using a two-step perturbation technique. Therefore, a discretization with  $15 \times 15$  nodes is used for all further analyses. Secondly, we carried out a nonlinear analysis of a simply supported square orthotropic plate. Geometric properties of this plate are  $a = b = 12$  in. and  $h = 0.138$  in. as well as its material properties are Young’s modulus  $E_1 = 3.0 \times 10^6$  psi,  $E_2 = 1.28 \times 10^6$  psi,  $G_{12} = G_{13} = G_{23} = 0.37 \times 10^6$  psi, and Poisson ratio  $\nu_{12} = 0.32$ . As shown in Fig. 4, the result of Shen [45] and solution of Zaghoul using classical plate theory (CPT) [46] differ from experimental results of Zaghoul and Kennedy [46], while the present result is in good agreement with Zaghoul and Kennedy. It is believed that the discrepancies of present results between other

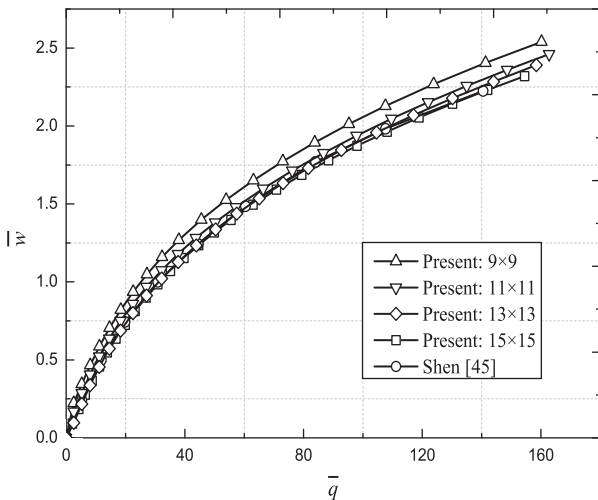


Fig. 3. Convergence property for simply supported square isotropic plate ( $\nu = 0.316$ ) under a uniformly distributed transverse load.

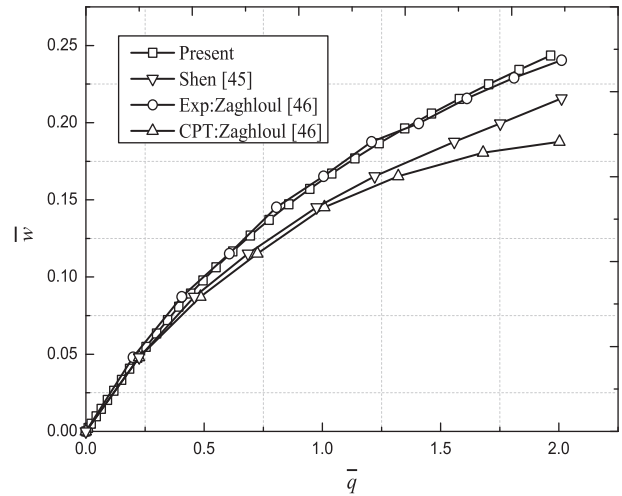


Fig. 4. Non-dimensional central deflection for simply supported square orthotropic plate.

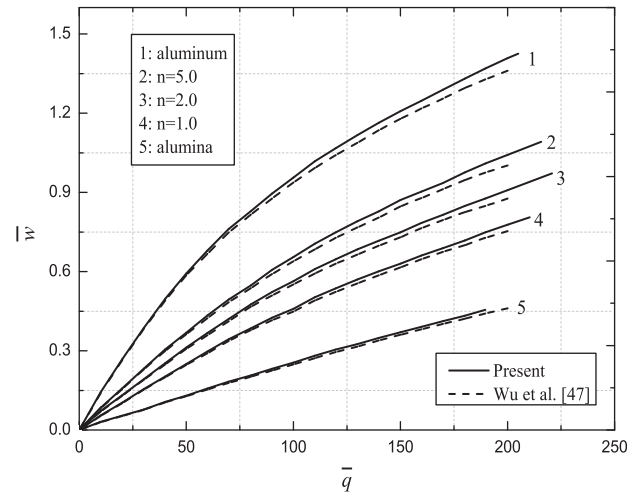


Fig. 5. Non-dimensional central deflection for clamped functionally graded square alumina/aluminum plates with different values of the volume fraction index  $n$ .

solutions are caused by different plate theories employed and the solution strategies used in the respective studies. Fig. 5 gives the non-dimensional load–deflection curves for a clamped functionally graded square alumina/aluminum plate with different values of the volume fraction index  $n$  of ceramic. Width-to-thickness ratio ( $b/h$ ) of the plate is set to 100 and material properties of the alumina/aluminum plate are  $E_c = 380$  GPa,  $E_m = 70$  GPa, and Poisson ratio is taken to be  $\nu = 0.3$ . It can be seen that the present results also match well with solutions of Wu et al. [47].

4.2. Linear analysis of CNTRC plates

In this section, a linear analysis of various types of CNTRC plates with different boundary conditions under a transversely uniformly distributed load  $q_0 = -0.1$  MPa is considered. For boundary conditions of the four edges of a plate, a sequence of letters containing “S”, “C” or “F”, is used to denote simply supported (S), fully clamped (C) or free (F), respectively. The thickness of the plates is taken to be 2.0 mm. Table 1 shows the non-dimensional central deflection  $\bar{w} = \frac{w_0}{h}$  for the UD and the other three types of FG–CNTRC square plates subjected to a uniform transverse load  $q_0$  with differ-

**Table 1**

Effects of width-to-thickness ratio ( $b/h$ ) on the non-dimensional central deflection  $\bar{w} = w_0/h$  for linear analysis of various types of CNTRC plates under different boundary conditions.

$b/h$		SSSS		CCCC		SCSC		SFSF	
		Present	FEM [17]						
10	UD	$3.751 \times 10^{-3}$	$3.739 \times 10^{-3}$	$2.233 \times 10^{-3}$	$2.228 \times 10^{-3}$	$3.333 \times 10^{-3}$	$3.325 \times 10^{-3}$	$3.449 \times 10^{-3}$	$3.444 \times 10^{-3}$
	FG-V	$4.479 \times 10^{-3}$	$4.466 \times 10^{-3}$	$2.360 \times 10^{-3}$	$2.351 \times 10^{-3}$	$3.860 \times 10^{-3}$	$3.853 \times 10^{-3}$	$4.191 \times 10^{-3}$	$4.186 \times 10^{-3}$
	FG-O	$5.245 \times 10^{-3}$	$5.230 \times 10^{-3}$	$2.517 \times 10^{-3}$	$2.512 \times 10^{-3}$	$4.441 \times 10^{-3}$	$4.433 \times 10^{-3}$	$4.973 \times 10^{-3}$	$4.967 \times 10^{-3}$
	FG-X	$3.188 \times 10^{-3}$	$3.177 \times 10^{-3}$	$2.114 \times 10^{-3}$	$2.109 \times 10^{-3}$	$2.874 \times 10^{-3}$	$2.867 \times 10^{-3}$	$2.910 \times 10^{-3}$	$2.905 \times 10^{-3}$
20	UD	$3.638 \times 10^{-2}$	$3.628 \times 10^{-2}$	$1.339 \times 10^{-2}$	$1.339 \times 10^{-2}$	$3.400 \times 10^{-2}$	$3.393 \times 10^{-2}$	$3.344 \times 10^{-2}$	$3.341 \times 10^{-2}$
	FG-V	$4.892 \times 10^{-2}$	$4.879 \times 10^{-2}$	$1.593 \times 10^{-2}$	$1.593 \times 10^{-2}$	$4.387 \times 10^{-2}$	$4.381 \times 10^{-2}$	$4.549 \times 10^{-2}$	$4.544 \times 10^{-2}$
	FG-O	$6.172 \times 10^{-2}$	$6.155 \times 10^{-2}$	$1.860 \times 10^{-2}$	$1.860 \times 10^{-2}$	$5.397 \times 10^{-2}$	$5.389 \times 10^{-2}$	$5.803 \times 10^{-2}$	$5.797 \times 10^{-2}$
	FG-X	$2.709 \times 10^{-2}$	$2.701 \times 10^{-2}$	$1.152 \times 10^{-2}$	$1.150 \times 10^{-2}$	$2.592 \times 10^{-2}$	$2.587 \times 10^{-2}$	$2.488 \times 10^{-2}$	$2.484 \times 10^{-2}$
50	UD	1.157	1.155	0.2614	0.2618	1.101	1.099	1.069	1.068
	FG-V	1.657	1.653	0.3643	0.3649	1.506	1.504	1.542	1.540
	FG-O	2.163	2.157	0.4719	0.4719	1.912	1.909	2.033	2.030
	FG-X	0.7921	0.7900	0.1892	0.1894	0.7728	0.7728	0.7338	0.7338

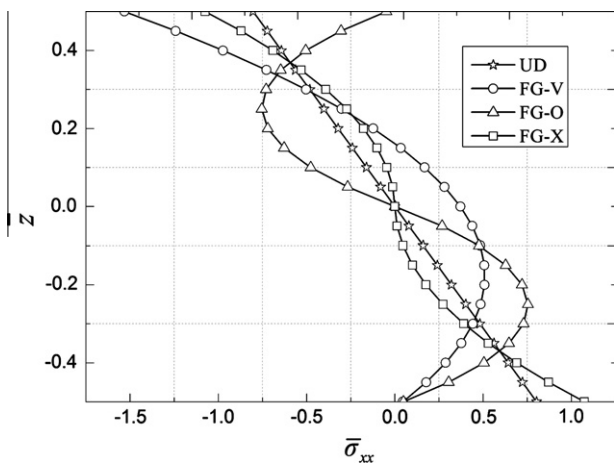


**Fig. 6.** Non-dimensional axial stress  $\bar{\sigma}_{xx} = \sigma_{xx}h^2/(q_0|a^2)$  in the CNTRC plates under a uniform load  $q_0 = -1.0 \times 10^5 \text{ N/m}^2$ .

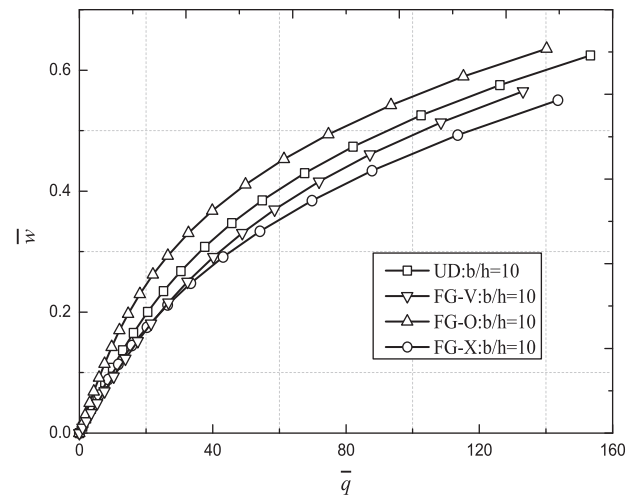


**Fig. 7.** Non-dimensional central deflection for various types of simply supported square CNTRC plates with plate width-to-thickness ratio of  $b/h = 10$ .

ent values of plate width-to-thickness ratio ( $b/h$ ) and different boundary conditions. It is found that the present results agree very well with solutions given by Zhu et al. using the finite element method [17]. Fig. 6 depicts the non-dimensional central axial stresses  $\bar{\sigma}_{xx} = \frac{\sigma_{xx}h^2}{|q_0|a^2}$  distributed along the non-dimensional thickness  $\bar{z} = \frac{z}{h}$  of various types of CNTRC plates with four edges simply supported subjected to a uniform transverse load  $q_0$  with volume fraction  $V_{\text{CNT}}^* = 0.11$  and width-to-thickness ratio  $b/h = 10$ . It can be found that the central axial stress distributions in UD, FG-O and FG-X CNTRC plates are zero at mid-plane and anti-symmetric about the mid-plane due to the symmetric reinforcements with respect to the mid-plane.

**4.3. Nonlinear analysis of CNTRC plates**

In this section, detailed parametric studies are carried out to investigate nonlinear behaviors of various types of CNTRC plates under transversely uniformly distributed loads. Non-dimensional parameters including  $\bar{w} = \frac{w_0}{h}$ ,  $\bar{z} = \frac{z}{h}$ ,  $\bar{\sigma}_{xx} = \frac{\sigma_{xx}h^2}{|q_0|a^2}$ , and  $\bar{q} = \frac{q_0a^2}{E_m h^3}$  are defined to describe the results. Several numerical examples are presented to reveal the effects of the CNT volume fraction, plate width-to-thickness, plate aspect ratio and boundary condition on the nonlinear response of various types of CNTRC plates.

Figs. 7–9 show variation in the non-dimensional central deflection with load for simply supported square UD- and the other three types of FG-CNTRC plates with different width-to-thickness ratios

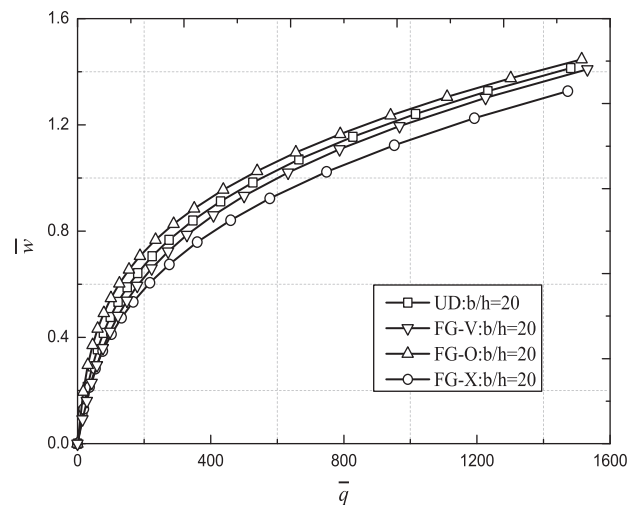


**Fig. 8.** Non-dimensional central deflection for various types of simply supported square CNTRC plates with plate width-to-thickness ratio of  $b/h = 20$ .

( $b/h = 10, 20, 50$ ) under a uniform transverse load. The CNT content by volume  $V_{\text{CNT}}^*$  is taken to be 0.11. It can be seen that the central deformation is smaller for the moderately thick CNTRC plate ( $b/h$

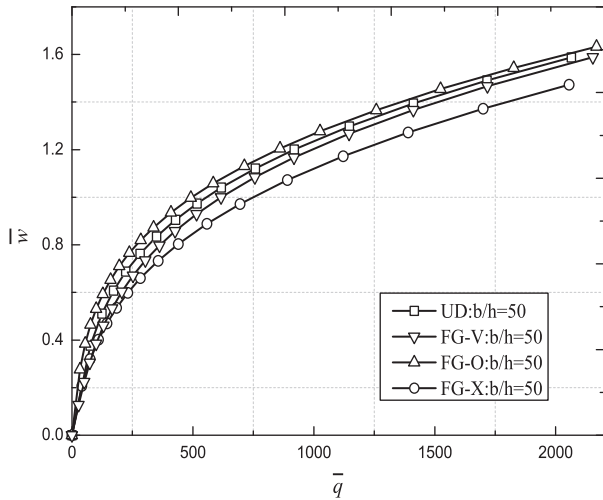


Fig. 9. Non-dimensional central deflection for various types of simply supported square CNTRC plates with plate width-to-thickness ratio of  $b/h = 50$ .

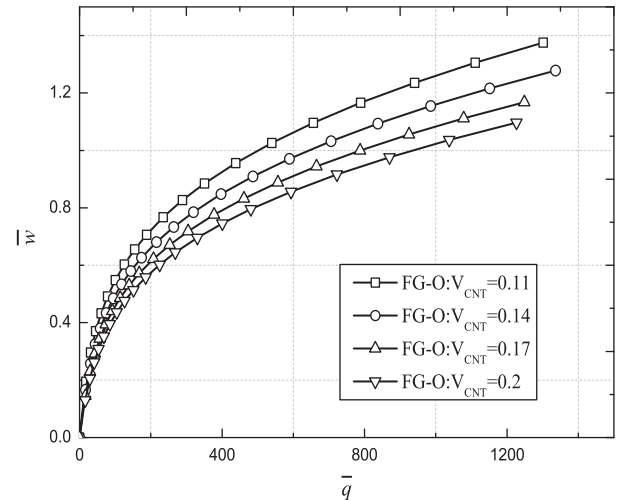


Fig. 12. Non-dimensional central deflection for simply supported square FG-O CNTRC plate with different values of CNT content by volume.

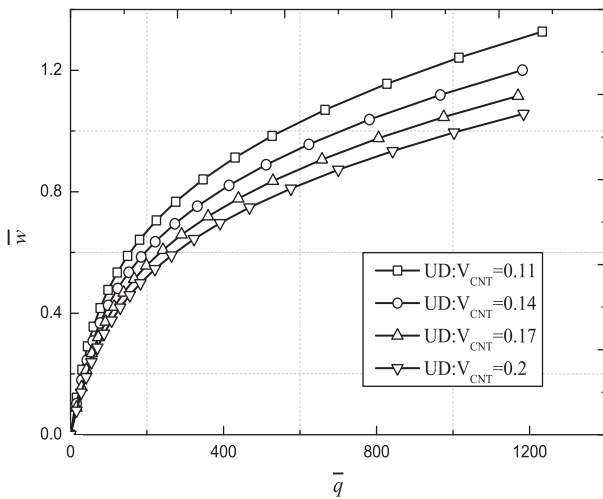


Fig. 10. Non-dimensional central deflection for simply supported square UD CNTRC plate with different values of CNT content by volume.

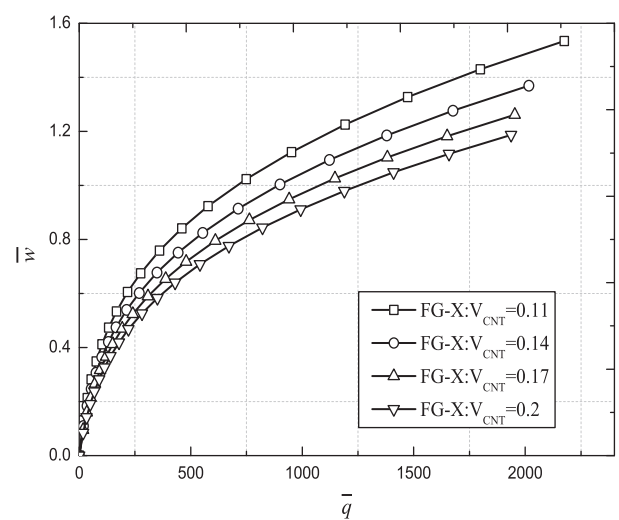


Fig. 13. Non-dimensional central deflection for simply supported square FG-X CNTRC plate with different values of CNT content by volume.

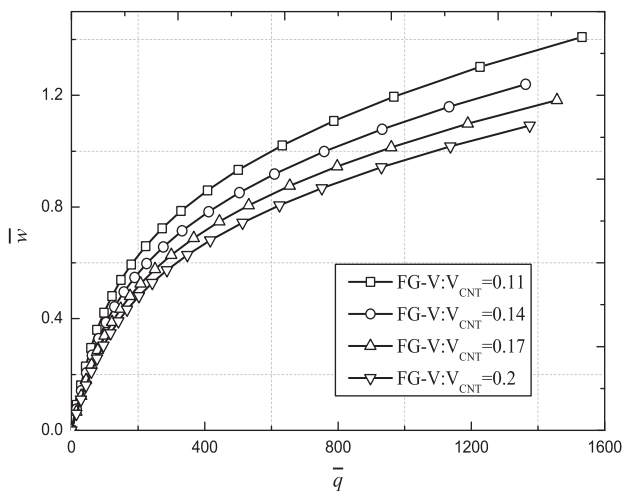
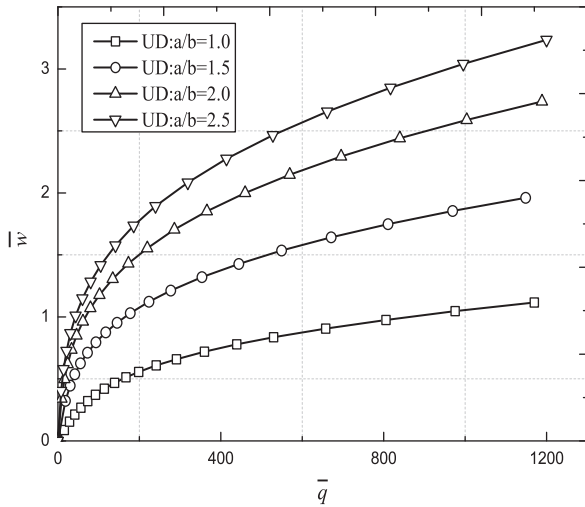


Fig. 11. Non-dimensional central deflection for simply supported square FG-V CNTRC plate with different values of CNT content by volume.

$h = 10$ ). It is worth to note that for these four types of CNTRC plates that have the same mass fraction of CNTs, FG-O plates have the largest values of the non-dimensional central deflection and the minimum values of the non-dimensional central deflection occurs for FG-X plates. We can conclude that CNTs distributed close to top and bottom surfaces are more efficient in increasing the stiffness of the plate than CNTs distributed near the mid-plane. Therefore, designers can obtain desired stiffness of CNTRC plates by regulating distributions of CNTs.

Figs. 10–13 show the non-dimensional load–deflection curves for simply supported square UD- and the other three types of FG-CNTRC plates with different values of the CNT content by volume ( $V_{CNT}^* = 0.11, 0.14, 0.17, 0.2$ ) under a uniform transverse load. The width-to-thickness ratios ( $b/h$ ) of the plates are set to 20. It can be observed that the non-dimensional central deflections of various types of CNTRC plates with different CNT content by volume rise as the load increases. We can also find that the non-dimensional central deflections for CNTRC plates that have a larger value of CNT content by volume increase at a lower rate since stiffness of CNTRC plate increases when the CNT content by volume increases.



**Fig. 14.** Non-dimensional central deflection for simply supported UD CNTRC plate with different plate aspect ratios.

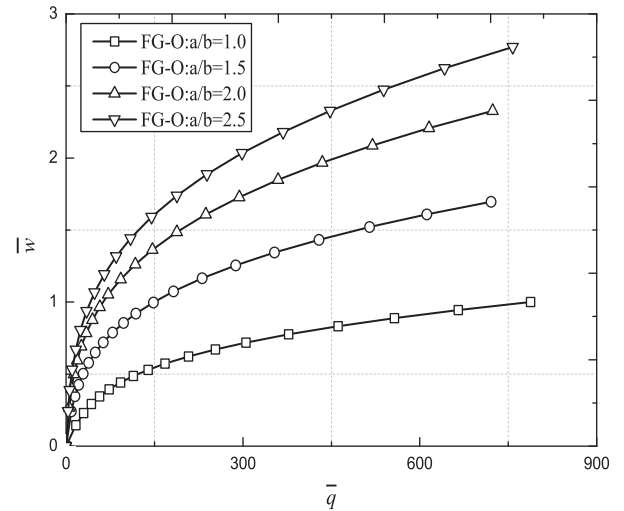


**Fig. 16.** Non-dimensional central deflection for simply supported FG-O CNTRC plate with different plate aspect ratios.

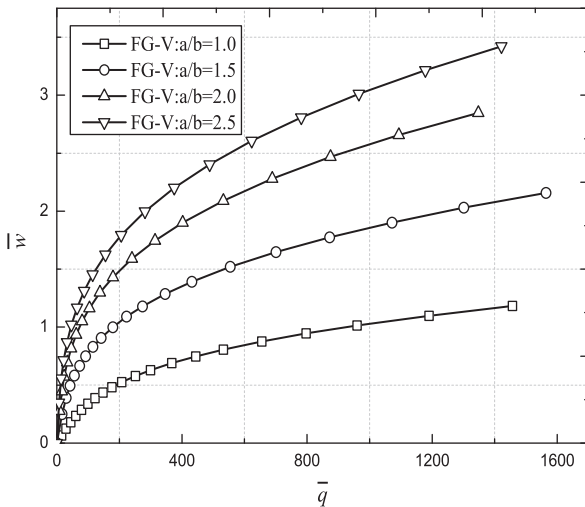


**Fig. 15.** Non-dimensional central deflection for simply supported FG-V CNTRC plate with different plate aspect ratios.

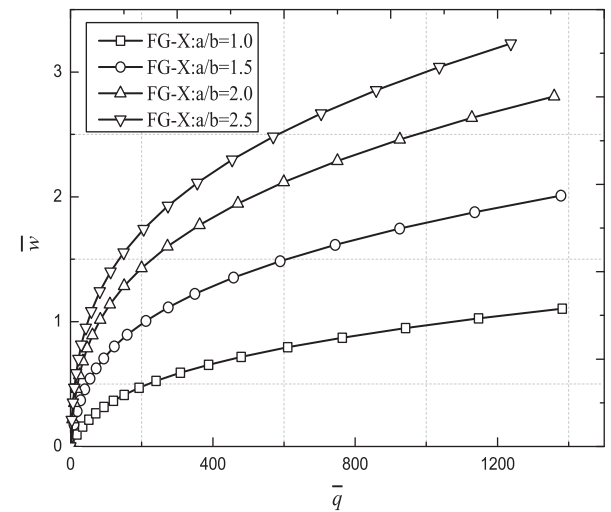


**Fig. 17.** Non-dimensional central deflection for simply supported FG-X CNTRC plate with different plate aspect ratios.

Compared the results in Figs. 7–9, a similar effect of the distribution types of CNTs in the plate can also be obtained.

Figs. 14–17 present the effect of plate aspect ratio ( $\beta = a/b = 1.0, 1.5, 2.0, 2.5$ ) on the nonlinear response of simply supported UD and the other three types of FG-CNTRC plates under a uniform transverse load. The CNT content by volume  $V_{CNT}^* = 0.17$  is considered and width-to-thickness ratio ( $b/h$ ) of the plates is chosen to be 20. It can be seen that central deflections are increased as plate aspect ratio  $\beta$  rises from 1.0 to 2.5. That is to be expected, because it is obvious that larger plate is easy to deform under transverse load. Compared the effect of CNT content by volume and plate width-to-thickness ratio, we can discover that the central deflection is more sensitive of plate aspect ratio than CNT content by volume and plate width-to-thickness ratio.

Figs. 18 and 19 depict non-dimensional load–deflection curves of square UD- and the other three types of FG-CNTRC plates subjected to a uniform transverse load with other two boundary conditions: four edges fully clamped (CCCC), two edges simply supported and two edges clamped (SCSC). The CNT content by volume ( $V_{CNT}^*$ ) and the width-to-thickness ratio ( $b/h$ ) are the same as

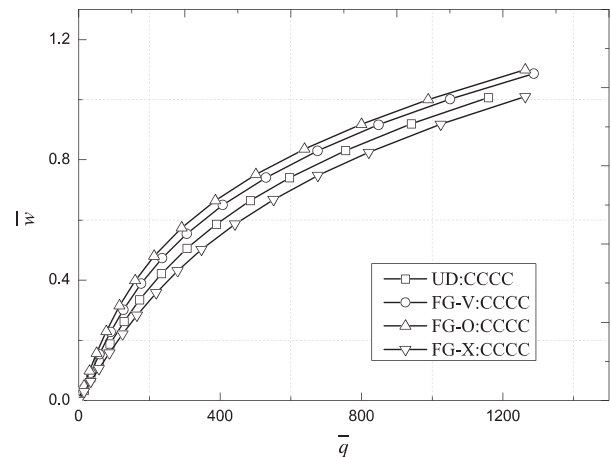


**Fig. 18.** Non-dimensional central deflection of various types of CNTRC plates with four edges fully clamped (CCCC).

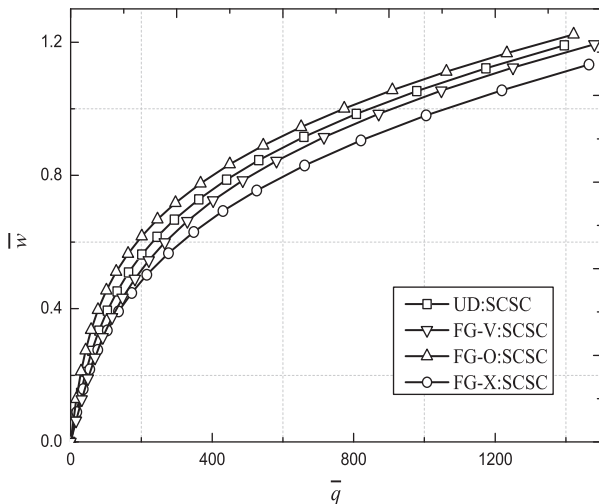


Fig. 19. Non-dimensional central deflection of various types of CNTRC plates with two edges simply supported and two edges clamped (SCSC).

those used before. The results show that the non-dimensional central deflections of four edges fully clamped (CCCC) CNTRC plates are larger than those of two edges simply supported and two edges clamped (SCSC) CNTRC plates, and values of the non-dimensional central deflections of SCSC CNTRC plates are higher than four edges simply supported CNTRC plates. The reason is that the constraint of clamped boundary condition is stronger than the simply supported boundary condition.

## 5. Conclusions

In this paper, nonlinear responses of various types of FG-CNTRC plates are studied using the element-free  $kp$ -Ritz method. Material properties of the plates are assumed to be graded in the thickness direction and effective material properties are estimated by Eshelby–Mori–Tanaka approach based on an equivalent continuum model. The nonlinear formulation is based on the FSDT, including von Kármán nonlinear terms, to account for small strains and moderate rotations. A set of kernel particle function is used to approximate two-dimensional displacement fields. The stabilized conforming nodal integration and direct nodal integration are employed to evaluate the bending stiffness and the shear as well as membrane stiffness so as to eliminate shear locking effect for very thin plates. Results reveal that the change of CNT content by volume, plate width-to-thickness, plate aspect ratios and boundary condition have pronounced effects on nonlinear responses of various types of CNTRC plates. The results also demonstrate that distribution types of CNTs significantly affect nonlinear behavior of CNTRC plates.

## Acknowledgements

The work described in this paper was fully supported by grants from the Research Grants Council of the Hong Kong Special Administrative Region, China (Project No. 9041674, CityU 118411) and the China National Natural Science Foundation (Grant No. 11172253).

## References

- [1] E.T. Thostenson, C. Li, T.W. Chou, Nanocomposites in context, *Compos. Sci. Technol.* 65 (2005) 491–516.
- [2] A.K.T. Lau, D. Hui, The revolutionary creation of new advanced materials—carbon nanotube composites, *Compos. Part B* 33 (2002) 263–277.
- [3] P.J.F. Harris, Carbon nanotubes and related structures: new materials for the twenty-first century, Cambridge University Press, 2001.
- [4] L. Bokobza, Multiwall carbon nanotube elastomeric composites: A review, *Polymer* 48 (2007) 4907–4920.
- [5] D. Qian, E.C. Dickey, R. Andrews, T. Rantell, Load transfer and deformation mechanisms in carbon nanotube-polystyrene composites, *Appl. Phys. Lett.* 76 (2000) 2868–2870.
- [6] P. Pötschke, T.D. Fornes, D.R. Paul, Rheological behavior of multiwalled carbon nanotube/polycarbonate composites, *Polymer* 43 (2002) 3247–3255.
- [7] J.D. Fidelus, E. Wiesel, F.H. Gojny, K. Schulte, H.D. Wagner, Thermo-mechanical properties of randomly oriented carbon/epoxy nanocomposites, *Compos. Part A* 36 (2005) 1555–1561.
- [8] V. Anumandla, R.F. Gibson, A comprehensive closed form micromechanics model for estimating the elastic modulus of nanotube-reinforced composites, *Compos. Part A* 37 (2006) 2178–2185.
- [9] Y. Han, J. Elliott, Molecular dynamics simulations of the elastic properties of polymer/carbon nanotube composites, *Comput. Mater. Sci.* 39 (2007) 315–323.
- [10] H.S. Shen, Postbuckling of nanotube-reinforced composite cylindrical shells in thermal environments, Part I: Axially-loaded shells, *Compos. Struct.* 93 (2011) 2096–2108.
- [11] H.S. Shen, Postbuckling of nanotube-reinforced composite cylindrical shells in thermal environments, Part I: Axially-loaded shells, *Compos. Struct.* 93 (2011) 2096–2108.
- [12] G. Formica, W. Lacarbonara, Eshelby-like equivalent continuum modeling of carbon nanotube-based composites, in: *Proceedings of 7th EUROMECH Solid Mechanics Conference*, Lisbon, September 2009.
- [13] D.L. Shi, X.Q. Feng, Y.Y. Huang, K.C. Hwang, H.J. Gao, The effect of nanotube waviness and agglomeration on the elastic property of carbon nanotube-reinforced composites, *J. Eng. Mater. Technol.* 126 (2004) 250–257.
- [14] X. Li, H. Gao, W.A. Scrivens, D. Fei, X. Xu, M.A. Sutton, A.P. Reynolds, M.L. Myrick, Reinforcing Mechanisms of Single-Walled Carbon Nanotube-Reinforced Polymer Composites, *J. Nanosci. Nanotechnol.* 7 (2007) 2309–2317.
- [15] H.S. Shen, Postbuckling of nanotube-reinforced composite cylindrical shells in thermal environments Part I: Axially-loaded shells, *Compos. Struct.* 93 (2011) 2096–2108.
- [16] M. Koizumi, The concept of FGM, *ceramic transactions, Funct. Gradient Mater.* 34 (1993) 3–10.
- [17] P. Zhu, Z.X. Lei, K.M. Liew, Static and free vibration analyses of carbon nanotube-reinforced composite plates using finite element method with first order shear deformation plate theory, *Compos. Struct.* 94 (2012) 1450–1460.
- [18] H.S. Shen, Nonlinear bending of functionally graded carbon nanotube-reinforced composite plates in thermal environments, *Compos. Struct.* 91 (2009) 9–19.
- [19] L.L. Ke, J. Yang, S. Kitipornchai, Nonlinear free vibration of functionally graded carbon nanotube-reinforced composite beams, *Compos. Struct.* 92 (2010) 676–683.
- [20] B.S. Aragh, A.H.N. Barati, H. Hedayati, Eshelby–Mori–Tanaka approach for vibrational behavior of continuously graded carbon nanotube-reinforced cylindrical panels, *Compos. Part B* 43 (2012) 1943–1954.
- [21] G. Formica, W. Lacarbonara, R. Alessi, Vibrations of carbon nanotube-reinforced composites, *J. Sound Vib.* 329 (2010) 1875–1889.
- [22] S.J. Mehrabadi, B.S. Aragh, V. Khoshkharesh, A. Taheripour, Mechanical buckling of nanocomposite rectangular plate reinforced by aligned and straight single-walled carbon nanotubes, *Compos. Part B* 43 (2012) 2031–2040.
- [23] H.S. Shen, Postbuckling of nanotube-reinforced composite cylindrical shells in thermal environments, Part I: Axially-loaded shells, *Compos. Struct.* 93 (2011) 2096–2108.
- [24] H.S. Shen, Postbuckling of nanotube-reinforced composite cylindrical shells in thermal environments, Part II: Pressure-loaded shells, *Compos. Struct.* 93 (2011) 2496–2503.
- [25] H.S. Shen, C.L. Zhang, Thermal buckling and postbuckling behavior of functionally graded carbon nanotube-reinforced composite plates, *Mater. Des.* 31 (2010) 3403–3411.
- [26] X. Zhao, Q. Li, K.M. Liew, T.Y. Ng, The element-free Ritz method for free vibration analysis of conical shell panels, *J. Sound Vib.* 295 (2006) 906–922.
- [27] K.M. Liew, J. Wang, M.J. Tan, S. Rajendran, Postbuckling analysis of laminated composite plates using the mesh-free  $kp$ -Ritz method, *Comput. Methods Appl. Mech. Eng.* 195 (2006) 551–570.
- [28] X. Zhao, K.M. Liew, T.Y. Ng, Vibration analysis of laminated composite cylindrical panels via a meshfree approach, *Int. J. Solids Struct.* 40 (2003) 161–180.
- [29] K.M. Liew, T.Y. Ng, X. Zhao, J.N. Reddy, Harmonic reproducing kernel particle method for free vibration analysis of rotating cylindrical shells, *Comput. Methods Appl. Mech. Eng.* 191 (2002) 4141–4157.
- [30] T. Mori, K. Tanaka, Average stress in matrix and average elastic energy of materials with misfitting inclusions, *Acta Metall.* 21 (1973) 571–574.
- [31] Y. Benveniste, A new approach to the application of Mori–Tanaka’s theory in composite materials, *Mech. Mater.* 6 (1987) 147–157.
- [32] T. Mura, *Micromechanics of defects in solids*, second ed., Martinus Nijhoff, The Netherlands, 1987.
- [33] J.N. Reddy, *Mechanics of Laminated Composite Plates and Shells: Theory and Analysis*, second ed., CRC Press, Boca Raton, FL, 2004.
- [34] E. Efraim, M. Eisenberger, Exact vibration analysis of variable thickness thick annular isotropic and FGM plates, *J. Sound Vib.* 299 (2007) 720–738.

- [35] J.S. Chen, C. Pan, C.T. Wu, W.K. Liu, Reproducing Kernel Particle Methods for large deformation analysis of non-linear structures, *Comput. Methods Appl. Mech. Eng.* 139 (1996) 195–227.
- [36] W.K. Liu, S. Jun, Y.F. Zhang, Reproducing kernel particle methods, *Int. J. Numer. Meth. FL* 20 (1995) 1081–1106.
- [37] S. Beissel, T. Belytschko, Nodal integration of the element-free Galerkin method, *Comput. Methods Appl. Mech. Eng.* 139 (1996) 49–74.
- [38] J.S. Chen, C.T. Wu, S. Yoon, Y. You, A stabilized conforming nodal integration for Galerkin mesh-free methods, *Int. J. Numer. Methods Eng.* 50 (2001) 435–466.
- [39] J. Dolbow, T. Belytschko, Numerical integration of the Galerkin weak form in meshfree methods, *Comput. Mech.* 23 (1999) 219–230.
- [40] T.C. Chang, J.Y. Geng, X.M. Guo, Chirality- and size-dependent elastic properties of single-walled carbon nanotubes, *Appl. Phys. Lett.* 87 (2005).
- [41] J.A. Elliott, J.K.W. Sandler, A.H. Windle, R.J. Young, M.S.P. Shaffer, Collapse of Single-Wall Carbon Nanotubes is Diameter Dependent, *Phys. Rev. Lett.* 92 (2004) 095501.
- [42] Y. Jin, F.G. Yuan, Simulation of elastic properties of single-walled carbon nanotubes, *Compos. Sci. Technol.* 63 (2003) 1507–1515.
- [43] K.M. Liew, J.W. Yan, Y.Z. Sun, L.H. He, Investigation of temperature effect on the mechanical properties of single-walled carbon nanotubes, *Compos. Struct.* 93 (2011) 2208–2212.
- [44] V.N. Popov, V.E.V. Doren, M. Balkanski, Elastic properties of crystals of single-walled carbon nanotubes, *Solid State Commun.* 114 (2000) 395–399.
- [45] H.S. Shen, Nonlinear bending of shear deformable laminated plates under transverse and in-plane loads and resting on elastic foundations, *Compos. Struct.* 50 (2000) 131–142.
- [46] S.A. Zaghoul, J.B. Kennedy, Nonlinear behavior of symmetrically laminated plates, *J. Appl. Mech.-Trans. ASME* 42 (1975) 234–236.
- [47] T.L. Wu, K.K. Shukla, J.H. Huang, Nonlinear static and dynamic analysis of functionally graded plates, *Int. J. Appl. Mech. Eng.* 11 (2006) 679–698.